Exploring the 3D printing of molybdenum carbide-based catalysts for the Reverse Water Gas Shift reaction: a multi scale study

Arturo Pajares[a,*], Jacob Andrade-Arvizu[b], Disha Jain[c], Matteo Monai[c,*], Jasper Lefevere[a], Pilar Ramírez de la Piscina[d], Narcís Homs[b,d], and Bart Michielsen[a]

[a]*Sustainable Materials, Flemish Institute for Technological Research (VITO NV), Boeretang 200, 2400 Mol, Belgium.*

[b]*Catalonia Institute for Energy Research (IREC), Jardins de les Dones de Negre 1, 08930 Barcelona, Spain.*

[c]*Inorganic Chemistry and Catalysis Group, Debye Institute for Nanomaterials Science and Institute for Sustainable and Circular Chemistry, Utrecht University, Universiteitsweg 99, 3584 CG Utrecht, The Netherlands.*

[d]*Departament de Química Inorgànica i Orgànica, Secció de Química Inorgànica and Institut de Nanociència i Nanotecnologia (IN2UB), Universitat de Barcelona, Martí i Franquès 1-11, 08028 Barcelona, Spain.*

[*]Corresponding author: Arturo Pajares (arturo.pajares@vito.be) and Matteo Monai (m.monai@uu.nl)

Keywords

Molybdenum carbide; 3D-printed catalysts; RWGS; transition metal carbides; CO_2 conversion.

ABSTRACT

A new methodology for preparing 3D printing molybdenum carbide-based catalysts with direct ink writing is presented. CO_2 conversion experiments through the reverse water gas shift reaction showed that the catalytic behavior of 3D-Mo_xC/Al_2O_3 catalysts is controlled by the crystallite size and crystalline phase, which in turn were dependent on the Mo loading. The formation of cubic δ-MoC and hexagonal η-Mo_3C_2 was prevalent in small crystallite sizes at low loading of Mo, and α/β-Mo_2C in larger crystallite sizes at high loading of Mo. *Operando* DRIFTS experiments points out that hydroxyl species present on the surface of Al_2O_3 play a

major role in bicarbonate formation that leads to the formation of formates, which eventually decomposes to CO and H_2O. The produced structures were mechanically stable and kept their structural and textural properties after reaction. Therefore, this work introduces new perspectives for scaling-up 3D printed structures based on molybdenum carbide.

1. Introduction

Over the past decades, CO_2 utilization has received renewed attention from researchers due to the CO_2 emissions rising. Converting CO_2, from detrimental greenhouse gas into value-added chemicals and fuels, provides an alternative to the transition to a low carbon economy, and a way to store renewable energy in the form of chemical bonds [1-4]. CO_2 can be first reduced to CO via the Reverse Water Gas Shift (RWGS) reaction ($CO_2 + H_2 \rightarrow CO + H_2O$; $\Delta_r H^o$ = 41.2 kJ mol^{-1} at 298 K), and subsequently CO can be used as feedstock to produce different chemicals and fuels [5,6]. Transition metal carbides (TMCs) have been used as alternative to conventional noble metal-based catalysts due to their similar catalytic properties [7,8]. Several TMCs can activate CO_2 and split H_2 considering them as feasible catalysts for CO_2 hydrogenation reactions [9-12]. Experimental and theoretical investigations demonstrated that molybdenum carbide shows the best catalytic behavior among the TMCs for the RWGS reaction [12-14]. MoC and Mo_2C have been the most studied TMC_S for CO_2 reduction [15-18], where the Mo:C ratio has been claimed as being a critical aspect in surface chemistry and catalysis [19]. Moreover, it has been shown that the presence of carbon vacancies in TMCs can play a key role in the RWGS reaction [20]. On the other hand, the deposition of the appropriate TMC active phase onto a support can be an interesting approach to improve the catalytic behavior of bulk TMCs materials, which usually show low surface area values [14-18]. Many investigations, in a laboratory scale, have been reported using powdered molybdenum carbide-based catalysts [14,16-18,21]. However, when the scale-up of a catalyst is contemplated, the powdered form is not appropriate and the manufacturing of catalysts with scalable methods and using low-cost materials is a main issue. After the optimal catalytic material is selected, engineering considerations related to the catalyst's incorporation into a reactor remain; more specifically the shaping of the catalytic material such as granules, pellets, extrudates or honeycomb monoliths are considered as established techniques [15]. Additive manufacturing or 3D printing of catalysts has only taken off in the last years as an attractive alternative to these conventional shaping technologies [22-26]. For the 3D structuring of catalysts, this technology holds a great potential, providing a very high degree of freedom in the design of catalysts, which allows the tailoring of 3D structures with specific operating windows and overcomes the limitations of conventional shaping methods. The 3D structures obtained from printing technology provides a better control of crucial process parameters such as minimizing mass transfer limitations and pressure drop in the reactor [24,25]. Moreover, they mitigate the formation of hot spots that are often found in conventional packed catalytic beds [26]. Recently,

some investigations have reported the use of 3D printing for the manufacturing of catalysts for different applications showing the obtained 3D-structures a better performance, higher stability, productivity, and selectivity to the desired compound [23,24]. So far, only few investigations in 3D-printing technology using 2D-TMCs (MXenes) have been reported for the fabrication of supercapacitors and electrodes [27-30]. To our knowledge, the use of 3D-printing technology for the fabrication of TMCs-based catalysts for thermochemical catalytic applications have not yet been reported. In this work, we present for the first time, the preparation, characterization, and catalytic application in the RWGS reaction of 3D printed catalysts based on molybdenum carbide. Additionally, we evidenced that the crystallization of molybdenum carbide particles and the phase transition are bounded to the Mo loading in samples, which determine the behavior of catalysts in the RWGS reaction, and the hydroxyl species present on the surface of Al_2O_3 play a major role in the reaction mechanism.

2. Experimental Section

2.1. Preparation

Preparation of MoO_3/Al_2O_3: Samples were prepared using $(NH_4)_6Mo_7O_{24}.4H_2O$ (Alfa Aesar®, 99%) and γ-Al_2O_3 (Sasol®, Puralox TH100/150) as Mo precursor and support, respectively, using a wet impregnation method in a rotary evaporator. The amounts of Mo precursor and Al_2O_3 for all samples were calculated based on the final loading of desired Mo (1-30 wt.%). Total Al_2O_3 corresponds to the amount of Al_2O_3 support (Puralox) and Al_2O_3 resulting from AlOOH (Sasol®, Disperal P2) dehydration, the latter was utilized as binder for the preparation of paste (next step). After impregnation, the samples were dried overnight and placed in an oven for calcination up to 623 K for the MoO_3/Al_2O_3 formation. Five samples were prepared (1MoAl, 5MoAl, 10MoAl, 20MoAl and 30MoAl with ca. 1, 5, 10, 20 and 30 Mo wt.%, respectively) using an optimized amount of Mo precursor, support, binder and HNO_3.

Preparation of pastes: The MoO_3/Al_2O_3 samples were milled and placed on a plastic flask. Then HNO_3 (0.63 M), methylcellulose (MC, 3.5 wt.%), and AlOOH (Disperal P2), used as binders, were added carefully. Weight ratio of Puralox/Disperal P2=4.1 was kept for all pastes. Weight ratios of (MoO_3/Al_2O_3+Disperal P2)/MC=3 and (MoO_3/Al_2O_3+Disperal P2)/HNO_3=1.4 were optimized for 20MoAl and 30MoAl pastes. The optimization of the paste corresponding to 5MoAl and 10MoAl was reached by increasing the amount of MC, (MoO_3/Al_2O_3+Disperal P2)/MC=2.2. For 1MoAl and 3D-Al_2O_3, the successful preparation

was reached by decreasing the amount of liquid phase, HNO_3, (MoO_3/Al_2O_3+Disperal P2)/HNO_3=2.1 and keeping the weight ratio of (MoO_3/Al_2O_3+Disperal P2)/MC=2.2. The exact amount of material used for the preparation of pastes is listed in Table S1. The pastes were stirred at 2000 rpm until a homogeneous paste was obtained using a planetary centrifugal mixer (ARE-250, Thinky Corp.). The pastes were kept at 273 K for 2 days to ensure a complete gelation and avoid water evaporation. Before printing, the rheology of the pastes was characterized.

Direct ink writing of the MoO_3/Al_2O_3 monoliths: The pastes were placed in a cylindrical container, then attached to a 3D-clay printer (Lutum 4.3, Vormvrij) (Figure S1). The design of the MoO_3/Al_2O_3 monolith can be found in Figure S2. In short, a standard design of (1-1) [22] was implemented in which layers were stacked on top of each other resulting in straight channels in the direction of the gas flow. A printing nozzle of 840 µm and compressed air (1-5 bar) were used. A demonstration of the 3D-printing procedure can be found in Supporting Movie. After the printing process, the MoO_3/Al_2O_3 monoliths were dried at room temperature for 3 days. 3D-Al_2O_3 monoliths were prepared for comparison according to the procedure described above followed by a thermal treatment up to 823 K (2.5 K min^{-1}) for 3 h under air in absence of Mo precursor.

Carburization of the MoO_3/Al_2O_3 monoliths: The MoO_3/Al_2O_3 monoliths were placed in a tubular furnace for thermal treatment under a CH_4/H_2/He=1/4/5 (molar ratio) atmosphere up to 1073 K (2.5 K min^{-1}) for 4 h, then cooled down to room temperature under He and exposed to air at this temperature without passivation; for Al_2O_3-supported molybdenum carbide catalysts, a detrimental effect of passivation with O_2 on the CO_2 hydrogenation has been reported [31].

2.2. Characterization

Characterization of powder: Prior characterization of samples, the 3D-structures were crushed and milled. Powder X-Ray diffraction patterns were scanned at room temperature in the 2θ range of 4º-100º, with a step width of 0.04º and counting 4 s at each step, using a PANalytical X'Pert PRO MPD diffractometer with a graphite monochromator and Cu Kα source (λ=1.5406 Å) at 40 kV and 40 mA. Phase identification was carried out using ICDD Powder Diffraction database. The Scherrer equation was utilized to calculate the crystallite size of the nanocrystallites of molybdenum carbide. The Mo and Al content in samples was determined

by inductively coupled plasma optical emission spectroscopy (ICP-OES, Agilent Technologies 5100). Transmission Electron Microscopy (TEM) images and energy dispersive X-ray analysis (EDX) were collected employing a JEOL J2010F microscope operated at an accelerating voltage up to 200 kV. Raman spectroscopy was performed with fHR-640 and iHR320 Horiba Jobin Yvon spectrometers coupled to a Raman probe detector and a CCD detector (cooled to 203 K). An excitation wavelength of 532 nm was employed in backscattering configuration. An excitation power of 1.7 mW was utilized to inhibit any thermal effects in the samples. The Raman shift was calibrated using a Si monocrystal reference and imposing the Raman shift for the main Si band at 520 cm^{-1}. X-ray photoelectron spectroscopy (XPS) analysis was performed using a Perkin Elmer PHI-5500 Multitechnique System (Physical Electronics) with an Al X-ray source (hν=1486.6 eV and 350 W). Samples were kept in an ultra-high vacuum chamber during acquisition (5.10^{-9}-2.10^{-8} Torr). The C 1s BE of adventitious carbon was determined in the same equipment and conditions using Au as reference. The BE values were referred to the mentioned above C 1s BE at 284.8 eV. The CasaXPS software was used for the component peak fitting. A Shirley-type background function was used to determine background contribution. The peak fitting was done using a few major constraints. The Mo 3d was deconvoluted into 4 doublets (Mo $3d_{5/2}$ – Mo $3d_{3/2}$) by fixing the Mo $3d_{5/2}$/Mo $3d_{3/2}$ area ratio to 1.5 and the Mo $3d_{5/2}$ – Mo $3d_{3/2}$ BE splitting at 3.1 eV. All the full width half maximum values of components were constrained. Gaussian-Lorentzian curves were used to fit all peaks and components.

N_2 adsorption-desorption isotherms were recorded at 77 K using an autosorb iQ2 MP instrument (Quantachrome GmgH). Prior to the measurements, the samples were outgassed at 473 K for 16 h to remove all adsorbed water from the samples. The specific surface area (S_{BET}) was calculated by multi-point BET analysis of N_2 adsorption isotherms. The pore size distribution was calculated applying the BJH method. H_2-Temperature Programmed Reduction (H_2-TPR) and CO_2-Temperature Programmed Desorption (CO_2-TPD) experiments were carried out using a Micromeritics AutoChem II 2920 chemisorption equipment. For H_2-TPR, the samples were pretreated at 363 K under He. After cooling to room temperature, the samples were exposed to a H_2/Ar (12 %v/v) flow and the temperature was increased up to 1073 K at 10 K min^{-1}. During reduction, the TCD signal was registered. For CO_2-TPD, the samples were first treated under a He flow for 15 min at 363 K and then with a H_2/Ar flow (12 %v/v) for 2 h at 573 K. Then, the temperature was cooled down to 308 K under a He flow and was maintained for 1 h at this temperature. After, the samples were contacted with a CO_2/He (10 %v/v) mixture for 1 h at 308 K and then purged under flowing He for 2 h. Finally, the CO_2-TPD profile was

recorded from 308 to 1073 K at 5 K min^{-1} under a He flow. During desorption, the TCD signal was also registered.

Characterization of 3D structures: Hg intrusion porosimetry was performed using two Thermo-Finnigan porosimeters (Pascal 140 and Porosimeter 2000 for the 4-100 um and 0.008-15 um diameter range, respectively). Measurements starts at vacuum up to 0.2 MPa, followed by measurement from 1 to 200 MPa. The density of samples was calculated using a Micromeritics AccuPyc II 1340 gas pycnometer. Morphological homogeneity and the infill patterns of the printed structures were examined by optical microscopy (OM). To do so, the fiber diameter was measured in different sections of each monolith. The images were acquired using a Zeiss Discovery V12 stereomicroscope, equipped with a Plan Apo S 1.0xFWD 60 mm objective and image collection performed using an Axiovision MRx digital camera connected to the microscope. Scanning electron microscopy (SEM) images, cross-section analysis, and energy dispersive X-ray (EDX) mapping were collected using a FEI Nova NanoSEM 450 instrument operating at an accelerating voltage up to 20 keV equipped with a Bruker QUANTAX 200 EDX system and an XFlash 6160 SDD detector. For cross-section SEM analysis, the structures were cut out in the middle and embedded under vacuum using a mixture of epoxy resin solutions (EpoFix Resin/Hardener). The mechanical strength of the manufactured structures was determined by crushing samples of 10.5 mm x 16.7 mm (w x h). A 100 kN measuring cell was used to detect the force needed to collapse the structures (model 5582, INSTRON).

Operando Diffuse Reflectance Infrared Fourier Transform Spectroscopy: To investigate the nature of the surface intermediates formed during CO_2 hydrogenation reaction, diffuse reflectance infrared Fourier transform spectroscopy (DRIFTS) experiments were performed over Al_2O_3, 5MoAl, 10MoAl and 30MoAl at 523, 573, 623 and 673 K. The 3D structures were crushed and pelletized to obtain granules of size 75-125 μm. DRIFTS experiments were performed in Bruker Tensor 37 Fourier Transform infrared (FT-IR) spectrometer equipped with liquid nitrogen cooled MCT detector. To perform the measurements, the Harrick's in situ DRIFTS cell was filled with the catalyst granules and was fitted in the Praying Mantis accessory, which was connected to the IR spectrometer. An internal thermocouple was installed in the catalyst bed to accurately control the temperature. Prior to the measurements, the catalyst was heated in 70 mL min^{-1} He flow at a ramp rate of 10 K min^{-1} to 673 K and reduced at this temperature under 70 mL min^{-1} H_2/He for 1 h; this pretreatment was done to reduce oxy-

carbides into carbides species before DRIFTS experiments. Afterwards, the sample was cooled to 523 K at 10 K min^{-1} and IR spectra were collected in 70 mL min^{-1} $CO_2/H_2/He$ (1/3/3) flow for 30 min to ensure steady state operation, hereafter the $CO_2/H_2/He$ (1/3/3) flow was stopped and IR spectra were recorded in H_2/He (3/4) flow for 30 min to identify the active and spectator species: the active species will react with H_2 and/or desorb, while spectator species will remain on the surface. The temperature was then raised in He flow to repeat the measurement at 573, 623 and 673 K. Additionally, IR measurements were also performed under 70 ml min^{-1} CO_2/He (1/4) and CO/He (1/4) flow at 308 and 523 K over 5MoAl to identify the surface adsorbates associated with adsorption of CO and CO_2.

Characterization of paste: Rheological characterization of the paste was made in a Thermo Haake MARS 60 instrument with 35 mm diameter parallel plates for oscillatory experiments, and 2^o angle cone and plate for the steady state experiments. For oscillatory experiments, the measurements were made by conditioning the paste for 10 min at a shear stress of 0.001 Pa using 2 % strain, followed by a shear stress swap between 0.001 Pa and 1000 Pa with 2 % strain. Steady state experiments were performed by conditioning the samples for 5 min with a shear rate of 0.01 s^{-1}. The shear rate was varied between 0.001 s^{-1} and 100 s^{-1}.

2.3. RWGS Catalytic tests

RWGS tests were performed in a quartz tube fixed bed reactor (i.d.=1.1 cm) placed in a Carbolite® furnace and connected to the steel tubing with the inlet capillary of the gas chromatograph. The printed structures were positioned in the center of the reactor with a thermocouple in direct contact. In all cases, one monolith (0.75-0.90 g) of catalyst was used. No pretreatment was performed prior to catalytic testing. The catalytic behavior in the RWGS reaction was studied in the temperature range of 523-873 K at 0.1 MPa. The fresh catalyst was heated from room temperature up to 523 K under N_2 flow and then exposed to a reactant gas mixture of $CO_2/H_2/N_2$=1/3/3 or 1/1/3 (molar ratio) with a total flow of 70 mL min^{-1} referred to a Gas Hourly Space Velocity (GHSV) of 4000 h^{-1}.

A long-term catalytic test (5 days) was carried out with the most performant catalyst at 873 K, using 0.75 g of catalyst, 0.1 MPa and a GHSV of 4000 h^{-1}, then the catalyst was characterized. In separate experiments, the RWGS was studied during 5 days at 4000 h^{-1}, and then the GHSV was increased to 8000, 12000 and 16000 h^{-1}, keeping a given GHSV value for 2 h. The variation of the GHSV was carried out by increasing the total inlet flow and keeping the reactant mixture

of $CO_2/H_2/N_2$=1/3/3 or 1/1/3 (molar ratio); 140, 210, and 280 mL min^{-1} of total inlet flow were used for values of GHSV of 8000, 12000 and 16000 h^{-1}, respectively.

The products were analyzed online with a gas chromatograph (Trace 1300 GC, Thermo Fisher Scientific), equipped with two TCDs and one FID detectors. Only CO and CH_4 were found as products. The carbon balance between the outlet gas and the reactant inlet was ≤ 1%. CO_2 conversion and product distribution were determined at each temperature by the average of 5 different analyses. The CO_2 conversion (X_{CO_2}) and the selectivity to the *i* product (S_i) were defined and obtained as follows:

$$X_{CO_2}(\%) = \left(1 - \frac{(C_{CO_2})_{outlet}}{(C_{CO_2})_{outlet} + \sum(C_i)_{outlet}}\right) \cdot 100 \quad (1)$$

$$S_i(\%) = \frac{(C_i)_{outlet}}{\sum(C_i)_{outlet}} \cdot 100 \quad (2)$$

where (C_i) and C_{CO_2} are the molar concentration of the *i* product (CO or CH_4) and CO_2, respectively.

3. Results and Discussions

In order to study the formation of molybdenum carbide, pure $(NH_4)_6Mo_7O_{24}.4H_2O$ and MoO_3 were carburized at 973, 1073 and 1173 K for 4 h (2.5 K min^{-1}) using a $CH_4/H_2/He$=1/4/5 (molar ratio) flow. The XRD patterns showed that a carburizing temperature of 973 K for both Mo precursors was not enough to obtain a pristine Mo_xC phase (Figure S3); in both cases the presence of MoO_2 (JCPDS 00-032-0671) can be inferred. However, samples prepared at 1073 and 1173 K only show the XRD peaks corresponding to the presence of Mo_2C (Figure S3). Although it is difficult to discern between orthorhombic α-Mo_2C (JCPDS 01-071-0242) and hexagonal β-Mo_2C (JCPDS 35-0787) due to the overlapping of their most intense XRD peaks, the orthorhombic α-Mo_2C phase can be deduced by the presence of low intensity peaks throughout entire range recorded (2θ=10-100º) (Figure S3); however, the simultaneous presence of β-Mo_2C cannot be ruled out. No other Mo_xC crystalline phases were detected. Additionally, the crystallite size of Mo_2C increased with the increase of carburization temperature.

The Mo_xC/Al_2O_3 monoliths were successfully synthesized by the 3D-printing approach described in the experimental section and Figure 1a; a carburizing temperature of 1073 K was used, which was established as optimum temperature for the molybdenum carbide preparation based upon the results above. The 3D-printed monoliths were prepared using a direct ink writing method in which a paste is passed through a thin nozzle which movement is controlled to deposit a pre-programmed fiber pattern (Supporting movie). The prepared pastes must flow easily through the nozzle and preserve their shape immediately after deposition [32,33].

Five samples were prepared as described in experimental section. All the prepared pastes showed similar viscosities and the desired shear thinning behavior spanning 4 decades in viscosity (Figure S4). An increase of the amount of liquid phase (HNO_3) was required for samples with higher MoO_3 loading to optimize the viscosity of pastes (Table S1); the pH of the pastes decreased with the increase of MoO_3 loading. A pH<5 accelerates the peptization of AlOOH [34,35]. This results in the formation of a gel of AlOOH that crosslink the particles of Al_2O_3 making a robust final 3D structure. Both, the storage modulus and the yield point of the 10MoAl and 30MoAl pastes, are higher compared to the Al_2O_3 reference (Table S2); this illustrates the modification of the characteristic of pastes when MoO_3 is incorporated into Al_2O_3.

The different pastes were all successfully printed through an 840 µm nozzle in the desired shape as shown in Figure S5. No deformation occurs during the subsequent drying process of the printed structures before the samples were carburized. After the carburization process of the printed MoO_3/Al_2O_3 structures, dark colored structures (w x h=10.5 mm x 16.7 mm) were obtained (Figure 1a,b and S5). OM analysis showed the architecture of the monoliths (Figure 1c and S6-S10), which were composed by fibers of a diameter consistent with the nozzle diameter used of the 3D-printer (840 µm), with homogeneous inter-fiber distance. The non-homogeneity within the fibers and throughout the monoliths could lead to an inhomogeneous gas flow of the reactants, hence a direct implication on the catalytic performance of the structures could be expected [22,36,37]. SEM analysis evidenced macropores and the presence of some cracks in the structures (Figure 1d and S6-S9). Important to note is that Al_2O_3 monoliths do not present any macropores or cracks (Figure S10). The presence of cracks and macroporosity might be the result of the carburization process of the structures during the preparation of Mo_xC/Al_2O_3 monoliths. SEM-EDX mapping analysis also showed the distribution of Mo_xC particles on Al_2O_3 (Figure 1e). The density of the structures increased with the presence of Mo_xC, due to the higher density of Mo_xC compared to Al_2O_3 (Table 1). The crush testing indicated good mechanical resistance of the structures for practical uses in

catalytic processes, where they are constantly subjected to stress and flow changes (Figure S11 and Table 1). It is noted that, the mechanical resistance of samples increases with the increasing of Mo_xC from 5MoAl (0.74 MPa) to 30MoAl (3.60 MPa), this might be associated to the higher crystallization of Mo_xC particles in the structures (Figures 1d and S7-S9). 1MoAl showed the highest mechanical resistance (3.68 MPa), this might be due to a lower presence of macropores and cracks compared to the other samples (Figure S6).

The N_2 adsorption-desorption isotherms and the corresponding pore size distributions of the prepared monoliths are shown in Figure S12. The S_{BET} values obtained for all structures were in the range of 102-160 $m^2\ g^{-1}$ (Table 1). As observed, all Mo_xC/Al_2O_3 monoliths showed a lower S_{BET} and higher pore volume values than Al_2O_3 monolith, this might be associated to the carburization process and the incorporation of Mo_xC particles onto the support. For 5MoAl-30MoAl samples, a higher incorporation of Mo produced a lower S_{BET} value, which was also reflected in the pore volume values (Table 1). All catalysts are mesoporous materials with average pore widths of 5.0-6.2 nm. However, as observed by SEM analysis, the samples showed a certain macroporosity as well. Therefore, Hg intrusion porosimetry tests were performed to analyze the macro/mesoporosity of samples in the pore range of 0.01-100 μm (Table 1 and Figure S13). All samples presented macro/mesopores in the range 0.01-0.1 μm. However, 5MoAl and 10MoAl clearly showed a bimodal pore distribution having also macropores in the range of 1-20 μm (Figure S13). The pore volume, measured by Hg intrusion, decreased with the increasing Mo loading from 5MoAl (0.81 $cm^3\ g^{-1}$) to 30MoAl (0.42 $cm^3\ g^{-1}$) samples, a similar trend as observed for the pore volume determined by N_2 isotherms detailed above (Table 1).

The XRD patterns of the Mo_xC/Al_2O_3 samples show a series of broad peaks at 2θ=31.9, 37.6, 39.5, 45.8, 60.5, 66.8 and 77.8º, which correspond to the support, cubic γ-Al_2O_3 (JCPDS 29-0063) (Figure 2a). For samples with a low loading of Mo, 1MoAl and 5 MoAl, it is difficult to discern the existence of crystalline Mo_xC phases; however, the presence of a shoulder at lower angles in the peak at 2θ=77.8º, might evidence the presence of a cubic δ-MoC phase (JCPDS 04-001-2968) in these two samples. For 10MoAl, the appearance of a broad peak at 2θ=41-44º and 72-77º could evidence the co-existence of cubic δ-MoC and hexagonal η-Mo_3C_2 (JCPDS 04-007-1465) phases. For 20MoAl and 30MoAl, the coexistence of δ-MoC, η-Mo_3C_2 and α/β-Mo_2C can be deduced. A higher intensity of the peaks corresponding to α/β-Mo_2C phase was observed when the Mo loading increased from 20MoAl to 30MoAl. Due to the low intensity and broad XRD peaks of Mo_xC in 1MoAl, 5MoAl and 10MoAl and the overleaping of Al_2O_3 XRD peaks; the crystallite size of Mo_xC was calculated only for 20MoAl and 30 MoAl, using

the peak at 2θ=52.1° of α/β-Mo_2C. A crystallite size of 12.7 and 19.0 nm was deduced for 20MoAl and 30MoAl, respectively. Finally, no crystalline MoO_x species were detected in any of the carburized samples.

TEM analysis of the Mo_xC/Al_2O_3 monoliths confirmed the presence of Mo_xC phases (Figure 1f and S6-S9). The mean particle size increased with the loading of Mo in samples. For 1MoAl, a small number of particles with size lower than 1 nm was observed (Figure S6), which can suggest the presence of δ-MoC: the formation of the cubic δ-MoC phase is thermodynamically favored at small particle sizes [15,16,38]. For 5MoAl, the mean particle size was 1.8 nm and only the δ-MoC phase was found (Figure S7). For 10MoAl, a mean particle size of 2.5 nm and the presence of δ-MoC and η-Mo_3C_2 were determined (Figure 1f), this is in well agreement with that deduced from XRD analysis. A bimodal particle size distribution is observed in 20MoAl (Figure S8) and 30MoAl (Figure S9). The second mode with a mean particle size of 11.9 nm and 18.5 nm for 20MoAl and 30MoAl, respectively, can be related to the presence of α/β-Mo_2C phase, which agrees well with the crystallite size of α/β-Mo_2C phase measured by XRD (Table 1). However, the first mode for both samples at lower particle size range, d_p=4.6 nm for 20MoAl and d_p=6.4 nm for 30MoAl, might be associated to the presence of δ-MoC and η-Mo_3C_2 phases. These observations are consistent with available literature concerning the preparation of different molybdenum carbide phases and theoretical predictions about the relationship between phase stability and Mo_xC crystallite size; the δ-MoC and η-Mo_3C_2 phases are prevalent in particles with small size and α/β-Mo_2C tend to predominate in large particles [17,38]. In addition to TEM analysis, STEM-EDX analysis showed a homogeneous distribution of Mo along the support (Figure 1g and S6-S9). SEM cross-section analysis of the samples with the lowest Mo loading (1MoAl) and the highest Mo loading (30MoAl) was performed to observe the distribution of elements into the structures (Figure 1h,i). In both cases, Mo_xC and Al_2O_3 coming from the binder dehydration (AlOOH) form a well disperse network around the Al_2O_3 puralox particles. This network likely makes the structure mechanically stable and robust. Moreover, the presence of macropores into the structure is observed.

H_2-TPR experiments (Figure 2b and Table S3) revealed a small H_2 consumption in the 519-632 K range corresponding to the reduction of oxy-carbide species [16-18]. The small peaks around 715-744 K indicated that MoO_3 is present in very low amount [39]. The presence of oxy-molybdenum species can be due to the exposition of the structures to air after the carburization. The peaks at higher temperature (1008-1040 K) can be associated to the reduction of molybdenum carbide species [40,41]. The H_2 consumption at this high temperature increases with the higher presence of Mo_xC from 0.002 (1MoAl) to 0.042

(30MoAl) mol_{H_2} g_{cat}^{-1}. However, when H_2 consumption is referred to Mo loading (mol_{H_2} mol_{Mo}^{-1}), 5MoAl showed the highest value of 0.048. This higher value can be attributed to a higher dispersion of Mo_xC on the support, which was determined by XPS as shown below.

The samples were further characterized by XPS. Figure 2c shows the Mo 3d core level spectra of the samples. The $3d_{5/2}$ peaks at low BE region, centered at 228.4-228.6 eV, are attributed to Mo^{2+} and/or Mo^{3+} in Mo_xC species [14-18]. From 5MoAl to 30MoAl, the $Mo^{2+,3+}/Mo^{n+}$ ratio increased with the Mo loading, according with the increase of the presence of Mo_2C (Table 2). The Mo $3d_{5/2}$ features centered at 230.0-230.5, 231.3-232.0 and 233.1-233.4 eV can be assigned to Mo^{4+}, Mo^{5+} and Mo^{6+}, respectively, which can be associated to molybdenum oxide and/or oxy-carbide species [14-18]; note that in H_2-rich conditions, such as RWGS reaction (CO_2/H_2=1/3), the surface molybdenum oxide and oxy-carbide species start reducing at temperatures above 593 K [42]. Figure S14 shows the spectra of C 1s, O 1s and Al 2p core levels of samples. The C 1s spectra of all samples (Figure S14a) show a broad peak with maximum at 284.8 eV associated to C-C bonds. The features at 283.5-283.7 eV are associated to C-Mo species, the shoulders at BE higher than 284.8 eV are related to the presence of carbon-oxygen species [16-18]. In O 1s spectrum of all samples (Figure S14b), a main peak with maximum located at 531.2 eV, associated to Al_2O_3, was found [16]. The bands at lower BE (529.5-530.0 eV) can be attributed to molybdenum oxy-species and that with BE higher than 531.2 eV to different oxygen-carbon bonded species [16-18]. In all cases, Al 2p spectrum corresponds well with the presence of Al_2O_3 (Figure S14c).

Table 2 shows the Mo content of catalysts and the Mo/Al molar ratio determined by ICP ($(Mo/Al)_{ICP}$), and XPS ($(Mo/Al)_{XPS}$). The Mo content obtained was near to the nominal value used for the preparation of the catalysts. $(Mo/Al)_{ICP}$ and $(Mo/Al)_{XPS}$ values increased from 1MoAl to 30MoAl due to the increase of Mo loading. From these parameters, a qualitative dispersion factor (D) can be calculated as follows [43].

$$D = \frac{(\mathrm{Mo/Al})_{XPS}}{(\mathrm{Mo/Al})_{ICP}} \qquad (3)$$

1MoAl, 5MoAl and 10MoAl showed a dispersion factor higher than 1 (Table 2), this means a higher relative presence of Mo on the surface than in the bulk. For samples 20MoAl and 30MoAl, a dispersion factor lower than 1 reflects a poorer dispersion of Mo on the surface (Table 2). This can be related to the higher crystallite size of Mo_xC in 20MoAl and 30MoAl,

compared to 1MoAl, 5MoAl and 10MoAl samples. The highest dispersion factor calculated for 5MoAl agrees with the H_2-TPR results shown above.

All samples showed low intensity Raman bands centered at 1343 and 1604 cm^{-1} (Figure S15), characteristic of carbonaceous species (D and G bands). Bands in the zone 100-1000 cm^{-1} due to the presence of MoO_x species were not found [16-18].

CO_2-TPD experiments were performed to analyze the basic properties of Mo_xC/Al_2O_3 structures. Figure S16 shows the CO_2 desorption profiles; for comparison, Al_2O_3 and pristine α-Mo_2C phase were also analyzed. All Mo_xC/Al_2O_3 samples exhibited a CO_2 desorption peak centered at 378 K, related with the presence of weak basic sites, which might be associated to δ-MoC and in a minor extension to Al_2O_3 [13,44,45]. At this low temperature, CO_2 desorption possibly can be related with the formation of functional groups such as carboxylic acid sites formed on surface [46]. The amount of desorbed CO_2 ($mmol_{CO_2}$ mol_{Mo}^{-1}) at this temperature decreases with increasing Mo loading (Table S4).

The peak in the CO_2-TPD profiles of 20MoAl and 30MoAl in the range of 920-1073 K can be ascribed to strong basic sites and associated to the presence of Mo_2C [44]. The higher CO_2 uptake corresponding to 30MoAl (34.0 μmol_{CO_2} mol_{Mo}^{-1}) with respect that of 20MoAl (3.0 μmol_{CO_2} mol_{Mo}^{-1}) can be related to the presence of a higher amount of α/β-Mo_2C in the former, according with XRD results. These results agree with the stronger adsorption of CO_2 onto Mo_2C than onto MoC, where adsorbed CO_2 undergo dissociation into CO and O at above 920 K. [44,46]

Figure 3 shows the catalytic performance of the Mo_xC/Al_2O_3 structures in the RWGS reaction at 0.1 MPa and 523-873 K, using a $CO_2/H_2/N_2$=1/3/3 (molar ratio) and GHSV of 4000 h^{-1} as described in experimental section. All Mo_xC/Al_2O_3 catalysts were active under the reaction conditions and showed a higher CO_2 conversion than the Al_2O_3 monolith. Surprisingly, the latter was active above 673 K. 10MoAl was the best performing catalyst reaching a CO_2 conversion value of 54 % at 873 K (Figure 3a). All catalysts were highly CO selective (near 100 %) above 573 K (Figure 3b). Besides CO, only very small amounts of CH_4 were formed. The maximum CO yield per mass of catalyst, was gained at 873 K on 10MoAl, reaching about 17.6 mol_{CO} kg_{cat}^{-1} h^{-1} (Figure 3c). However, 1MoAl showed the highest CO yield based on Mo content (mol_{CO} mol_{Mo}^{-1} h^{-1}) in the whole temperature range studied (Figure 3d). The values of mol_{CO} mol_{Mo}^{-1} h^{-1} produced at 873 K were the following: 1MoAl (100.3) > 5MoAl (35.6) > 10MoAl (19.4) > 20MoAl (7.9) > 30MoAl (4.5). However, we must consider the contribution of the support in these catalysts which produces CO at high temperatures (Figure 3a).

In order to avoid thermodynamic equilibrium limitations, a GHSV of 12000 h^{-1} was used to determinate the apparent activation energy (E_a), which was carried out for 10MoAl and 30MoAl (Figure S17). The different characteristics of 10MoAl and 30MoAl are also reflected in the apparent activation energy (E_a), being 27 ± 1 and 22 ± 1 kJ mol^{-1} for 10MoAl and 30MoAl respectively. Both apparent E_a values are much lower than that reported in literature for different type of catalysts (powdered form) (Table S5). The slightly lower apparent E_a value obtained for 30MoAl compared to 10MoAl might be associated to the presence of Mo_2C phase in the former. Mo_2C can adsorb CO_2 more strongly, and thus lower the activation energy barrier with respect to δ-MoC and η-Mo_3C_2. However, the higher CO yield obtained over 10MoAl, can be related to other factors such as a small crystallite size and a higher dispersion of Mo_xC phases on the support.

10MoAl was also tested using a stoichiometric reactant mixture $CO_2/H_2/N_2$=1/1/3 (molar ratio). As expected, the CO_2 conversion values were lower compared to those obtained when a CO_2/H_2=1/3 (molar ratio) was used (Figure S18a). At 873 K, a CO_2 conversion value of 26 % was reached (lower than that of 54 % obtained using a CO_2/H_2=1/3). The CO selectivity was slightly higher in all temperature range when CO_2/H_2=1/1 instead of CO_2/H_2=1/3 was employed (Figure S18b), being the difference higher for lower reaction temperatures.

Post-reaction Mo_xC/Al_2O_3 monoliths did not show relevant structural and textural changes according to XRD and N_2 adsorption-desorption isotherms (Figure S19-S21 and Table S6). Mo_xC crystallite sizes of used Mo_xC/Al_2O_3 catalysts remain similar to those of the corresponding fresh catalysts. No modifications of the textural properties of the 3D printed monoliths after reaction were observed.

In order to check the stability of the most performant catalyst, 10MoAl, a long-term catalytic test was performed at 873 K, using a CO_2/H_2=1/3, for 5 days (Figure 3e). A gradual and slight deactivation was observed in the first 60 h, CO_2 conversion decreased from 50 % (1 h) to 41 % (60 h). Afterwards, no significant changes in the catalytic behavior of 10MoAl were found during the next 65 h. The CO selectivity remained steady near 100 % during the 5 days. The characterization of 10MoAl after the long-term catalytic test using XRD, N_2 adsorption-desorption isotherms and SEM indicated the structural and textural stability of the catalyst (Figure S22).

In separate experiments, fresh 10MoAl was tested at 873 K under different GHSV (4000, 8000 12000 and 16000 h^{-1}) and 1/3 or 1/1 CO_2/H_2 molar ratios, following the experimental procedure described in experimental section. Results obtained are depicted in Figure 4. As expected, for both reactant molar ratios, CO_2 conversion decreased when GHSV increased. However, the

CO production increased with the increase of GHSV. Values of 27.9 and 23.1 $mol_{CO}\ kg_{cat}^{-1}\ h^{-1}$ were obtained for a CO_2/H_2 molar ratio of 1/3 and 1/1, respectively, at a GHSV of 16000 h^{-1}. The CO selectivity was maintained near 100 % after 5 days under all reaction conditions used. To gain insights into the RWGS reaction mechanism over molybdenum carbide-based catalysts, operando DRIFT spectra were acquired under RWGS conditions (CO_2/H_2/He=1/3/3 and 523–673 K) over Al_2O_3, 5MoAl, 10MoAl and 30MoAl catalysts (Figure 5 and S23). Additionally, similar DRIFTS measurements were also performed over α/β-Mo_2C and δ-MoC to understand the reaction mechanism over the different Mo_xC phases; results are shown in Figure S23e and f, respectively. Figure 5 shows DRIFT spectra corresponding to Al_2O_3 and 5MoAl under RWGS conditions, IR bands from adsorbed species were observed in the region 1200-1800 cm^{-1}. These bands were attributed to the O-C-O vibrations and indicated the presence of majorly three types of surface species: i.e. carbonates (ν_{as}(OCO) =1471 cm^{-1}, ν_s(OCO) = 1361 cm^{-1}), bicarbonates (ν_{as}(OCO) =1650 cm^{-1}, ν_s(OCO) = 1440 cm^{-1}) , δ(O-H) = 1230 cm^{-1}), and formates (ν_{as}(OCO) =1590 cm^{-1}, ν_s(OCO) = 1375 cm^{-1}, δ(C-H) = 1390 cm^{-1}) [47-50]. It should be noted that no carbonyl (CO_{ads}) bands were observed in the region above 1800 cm^{-1} for any of the samples, consistently with the high selective production of $CO_{(g)}$ - (Figure 3b); CO is preferentially desorbed instead of reacting further via hydrogenation pathways (to e.g. CH_4). To confirm this, DRIFT spectra of 5MoAl under CO_2 and CO flow were recorded at 308 and 523 K (Figure S24). The formation of bicarbonate species was observed at 308 K under CO_2 flow; however, no surface species were observed over 5MoAl under CO flow. At 523 K, a small distortion in the CO band was observed at ~ 2118 cm^{-1}, however, it disappears at the same rate as $CO_{(g)}$ when was purged with He and hence, it may be associated with physisorbed CO species.

In the case of Al_2O_3, under RWGS at low temperatures (523–573 K), only bicarbonate species were observed (Figure 5a). These species were formed by the reaction of $CO_{2(g)}$ with surface hydroxyls on Al_2O_3 surface. At 623 K, the presence of formate species was also determined, indicating the partial conversion of bicarbonates to formates. This conversion was further promoted at 673 K, where formates were the most abundant species on the surface of Al_2O_3. This can be related with the activation of H_2 over Al_2O_3, which is hindered at low temperature (573 K) [50]; however, as the temperature was raised, the increase in H_2 dissociation rate led to reduction of bicarbonates to formates. This was confirmed by experiments in which the gas composition was switched from CO_2 + H_2 to H_2 at different temperatures, where the bicarbonate signals were completely removed under H_2 at 623 K (Figure 5a).

Operando DRIFT spectra of 5MoAl in CO_2 + H_2 flow showed different spectral features in comparison to Al_2O_3 (Figure 5 and S25). Over 5MoAl, formates were formed at all temperatures, while bicarbonates species were observed only at low temperature, see the shoulder on the formate bands around 1650 cm^{-1} (Figure 5b). The broadness of the 1550–1700 cm^{-1} band reduced upon switching from CO_2 + H_2 to H_2 (Figure 5b), indicating the conversion of bicarbonates to formates [49] already at 523 K. This is consistent with the low barrier for H_2 activation over Mo_xC, which promotes bicarbonate hydrogenation [10]. At 673 K, a significant reduction in formate bands was observed upon switching from CO_2 + H_2 to H_2 flow indicating instability or conversion of formates at this temperature. Additionally, some carbonates species (band at 1471 cm^{-1}) were observed on 5MoAl surface at 523 K, which vanished as the temperature was raised and also decreased in concentration upon switching to H_2 flow (Figure 5b). We propose that the carbonate species formed on molybdenum oxy-carbide, and they decomposed as the temperature was increased. Operando DRIFTS experiments indicated that the formation of carbonates over 5MoAl under CO_2 + H_2 mixture, was more pronounced when a He pretreatment was carried out with respect to a H_2 pretreatment, as shown in Figure S26 (See supplementary material for further discussion).

Notably, both on Al_2O_3 and 5MoAl, the formation of formate species was accompanied with the evolution of $CO_{(g)}$, indicating that formates were either involved in the rate determining step of the reaction, or formed as spectator species in a side reaction which was also activated by H*. Additionally, 5MoAl, 10MoAl and 30MoAl showed a higher evolution of $CO_{(g)}$ band with respect to Al_2O_3, being 10MoAl the most performant (Figure S27). Moreover, the pristine δ-MoC showed a higher $CO_{(g)}$ band than α/β-Mo_2C. This information is consistent with the higher catalytic activity of 10MoAl where the δ-MoC phase is predominant (Figure 3a). Figure S28 depicts the change in the surface species over 5MoAl under CO_2 and CO_2+H_2 flow at 523 K. During CO_2 flow, the surface of 5MoAl is primarily covered by bicarbonate species and upon switching to CO_2+H_2 flow, the conversion of bicarbonates to formates can be clearly seen. It is also interesting to note the difference in the asymmetric and symmetric OCO stretching of bicarbonate species over Al_2O_3 and 5MoAl under CO_2+H_2, which can be due to the change in the nature of active site on loading Mo_xC on Al_2O_3.

Previous studies reported formates to be both spectator and reactive species in the RWGS reaction [50,51]. However, since the formate species were (i) not removed under H_2 on Al_2O_3, (ii) remained unchanged with temperature over 5MoAl, and (iii) were only removed in H_2 at 673 K, we suggest that the observed formates are spectator species in the reaction at temperatures below 673 K. Our observations highlight the role of bicarbonate as an active

reaction intermediate in RWGS over Mo_xC/Al_2O_3 and suggest that the rate determining step of this reaction mechanism is either the hydrogenation of bicarbonates to highly reactive formates, which further decompose to CO, or the spillover of H* to the bicarbonate species (Figure 6). Moreover, Figure S23 indicates that no surface intermediates were observed in α/β-Mo_2C, δ-MoC as well as over higher-loading 10MoAl and 30MoAl catalysts under the RWGS reaction conditions. This might indicate that the decomposition rate of formates will increase on higher Mo_xC loading samples leading to higher CO production as the availability of H* increases (Figure S27). However, a decrease in catalytic activity was observed when the Mo_xC loading was increased beyond 10 wt.%, which can be due to a lower amount of precursor for bicarbonate formation i.e. a diminution in the number of Al_2O_3 surface hydroxyl groups is expected for Mo_xC/Al_2O_3 with high Mo_xC loading. On the other hand, over high Mo_xC loading catalysts, mainly the redox mechanism could take place, such as has been found by DFT calculations for bulk Mo_xC systems [18,31,52-54].

DFT studies on Mo_4C_2 cluster suggested that the formation of formates by reaction between CO_2* and H* exhibits higher activation energy compared to redox pathway, wherein the dissociative adsorption of CO_2 results in the CO* and O* formation by producing the corresponding oxy-carbide species, subsequently hydrogenation of this surface oxy-carbide species results in Mo_xC and H_2O formation [53] However, the effect of surface hydroxyls on reaction mechanism was not investigated in the DFT study. In the present study, it is demonstrated from DRIFTS operando studies that the surface hydroxyl species present on the surface of Al_2O_3 play a major role in bicarbonate formation that leads to the formation of formates, which eventually decomposes to CO and H_2O. In this context, we could propose that for small particles of Mo_xC the extent of interface between Mo_xC and Al_2O_3 would be higher compared to that of larger Mo_xC particles, and thus could favor the associative pathway. The redox mechanism would be favored over large Mo_xC particles, as has been shown for bulk Mo_2C [18] (Figure 6). Although adsorbed CO species over higher-loading 10MoAl and 30MoAl catalysts, were not observed in the present study, the redox mechanism cannot be disproved. Future studies should focus on understanding the role of H* spillover in RWGS on molybdenum carbide-based catalysts, by varying the extent of the Mo_xC/Al_2O_3 interface, the Mo_xC interparticle distance and the OH population of the support.

Conclusions

The manufacturing of 3D-printed catalysts based on molybdenum carbide is presented for the first time. Mo_xC/Al_2O_3 monoliths with Mo loadings (1-30 wt.%) were successfully prepared.

The obtained 3D Mo_xC/Al_2O_3 structures were robust, meso/macro-porous, had large specific surface areas and showed high catalytic activities and CO selectivity in the RWGS reaction. Different phases and crystallite sizes of Mo_xC were obtained according to the Mo loading in the 3D structure. XRD and TEM analysis revealed that the formation of cubic δ-MoC and hexagonal η-Mo_3C_2 is prevalent in small particle sizes and α/β-Mo_2C in larger particle sizes. The Mo_xC/Al_2O_3 prepared with a ~10 wt.% of Mo (10MoAl), which presented a mixture of δ-MoC and η-Mo_3C_2 phases, showed the highest CO production (17.6 mol_{CO} kg_{cat}^{-1} h^{-1} at 873 K, 0.1 MPa and a GHSV of 4000 h^{-1}) and displayed a high stability after 5 days under reaction. Moreover, we investigated by operando DRIFTS the RWGS reaction mechanism over Mo_xC/Al_2O_3 systems, where reactive intermediates involved in the associative pathway (formate formation) were observed playing a key role in the CO formation. The characterization of the structures after reaction did not show significant changes respect to the fresh structures proving one of the advantages of this 3D-printed shaping technology. Therefore, this work offers new insights into the manufacturing of 3D printed structures based on molybdenum carbide and it opens new perspectives for scaling-up this kind of catalysts for CO_2 reduction processes on an industrial scale. This strategy can be extended to other TMCs by choosing appropriate metal precursors as starting materials, and for other catalytic applications.

Declaration of competing interest

The authors declare no competing interests.

Contributions

Arturo Pajares: Conceptualization, Methodology, Validation, Formal analysis, Investigation, Writing-Original draft, Writing – review & editing, Project administration. **Jacob Andrade-Arvizu**: Methodology, Formal analysis, Validation, Investigation. **Disha Jain:** Methodology, Formal analysis, Validation, Investigation. **Mateo Monai:** Methodology, Validation, Resources, Writing-review & editing, Supervision. **Pilar Ramírez de la Piscina:** Methodology, Resources, Writing-review & editing, Supervision. **Narcís Homs:** Methodology, Resources, Writing-review & editing, Supervision. **Jasper Lefevere:** Methodology, Resources, Writing-review & editing, Supervision, Project administration,

Funding acquisition. **Bart Michielsen:** Methodology, Validation, Resources, Writing-review & editing, Supervision, Project administration, Funding acquisition.

Acknowledgments

The authors gratefully acknowledge the technical assistance for characterization techniques to M. Mertens (XRD), A. De Wilde (Hg intrusion and He pycnometry), R. Kemps (SEM) and F. Beutels (ICP-AES) from VITO, K. Leyssens (N_2 sorption) from University of Antwerp, A. Llorente (H_2-TPR and CO_2-TPD) form IREC and Dr. Lluís Lopez-Conesa (TEM) and Dr. Lorenzo Calvo (XPS) from the scientific and technological centers of University of Barcelona (CCiTUB). N. Homs, and P. Ramirez de la Piscina thank the PID2020-116031RB-I00 project from MCIN/AEI/10.13039/501100011033/FEDER for financial support.

REFERENCES

[1] C. Hepburn, E. Adlen, J. Beddington, E.A. Carter, S. Fuss, N.M. Dowell, J.C. Minx, P. Smith, C.K. Williams, The technological and economic prospects for CO_2 utilization and removal, Nature 575 (2019) 87-97. https://doi.org/10.1038/s41586-019-1681-6

[2] J. Artz, T.E. Müller, K. Thenert, J. Kleinekorte, R. Meys, A. Sternberg, A. Bardow, W. Leitner, Sustainable conversion of carbon dioxide: An integrated review of catalysis and life cycle assessment, Chem. Rev. 118 (2018) 434-504. https://doi.org/10.1021/acs.chemrev.7b00435

[3] O.S. Bushuyev, P. De Luna, C.T. Dinh, L. Tao, G. Saur, J. Van de Lagemaat, S.O. Kelley, E.H. Sargent, What should we make with CO_2 and how can we make it?, Joule 2 (2018) 825-832. https://doi.org/10.1016/j.joule.2017.09.003

[4] J. Schneider, H. Jia, J. Muckerman, E. Fujita, Thermodynamics and kinetics of CO_2, CO, and H^+ binding to the metal centre of CO_2 reduction catalysts, Chem. Soc. Rev. 41 (2012) 2036-2051. https://doi.org/10.1039/C1CS15278E

[5] Y.A. Daza, J.N. Kuhn, CO_2 conversion by reverse water gas shift catalysis: comparison of catalysts, mechanism, and their consequences for CO_2 conversion to liquid fuels, RSC Adv. 6 (2016) 49675-49691. https://doi.org/10.1039/C6RA05414E

[6] J. Wei, Q. Ge, R. Yao, Z. Wen, C. Fang, L. Guo, H. Xu, J. Sun, Direct converting CO_2 into a gasoline fuel, Nat. Commun. 8 (2017) 15174. https://doi.org/10.1038/ncomms15174

[7] J.H. Sinfelt, D.J.C. Yates, Effect of carbiding on the hydrogenolysis activity of molybdenum, Nat. Phys. Sci. 229 (1971) 27-28. https://doi.org/10.1038/physci229027b0

[8] R.B. Levy, M. Boudart, Platinum-like behavior of tungsten carbide in surface catalysis, Science 181 (1973) 547-549. https://doi.org/10.1126/science.181.4099.547

[9] H. Zhou, Z. Chen, E. Kountoupi, A. Tsoukalou, P.M. Abdala, P. Florian, A. Fedorov, C.R. Müller, Two-dimensional molybdenum carbide 2D-Mo_2C as a superior catalyst for CO_2 hydrogenation, Nat. Commun. 12 (2021) 5510. https://doi.org/10.1038/s41467-021-25784-0

[10] H. Prats, J.J. Piñero, F. Viñes, S.T. Bromley, R. Sayós, F. Illas, Assessing the usefulness of transition metal carbides for hydrogenation reactions, Chem. Comm. 55 (2019) 12797-12800. https://doi.org/10.1039/C9CC06084G

[11] S. Posada-Pérez, F. Viñes, R. Valero, J.A. Rodriguez, F. Illas, Adsorption and dissociation of molecular hydrogen on orthorhombic β-Mo_2C and cubic δ-MoC (001) surfaces, Surf. Sci. 656 (2017) 24-32. https://doi.org/10.1016/j.susc.2016.10.001

[12] W. Wan, B.M. Tackett, J.G. Chen, Reactions of water and C1 molecules on carbide and metal-modified carbide surfaces, Chem. Soc. Rev. 46 (2017) 1807-1823. https://doi.org/10.1039/C6CS00862C

[13] C. Kunkel, F. Viñes, F. Illas, Transition metal carbides as novel materials for CO_2 capture, storage, and activation, Energy Environ. Sci. 9 (2016) 141-144. https://doi.org/10.1039/C5EE03649F

[14] M.D. Porosoff, S. Kattel, W. Li, P. Liu, J.G. Chen, Identifying trends and descriptors for selective CO_2 conversion to CO over transition metal carbides, Chem. Commun. 51 (2015) 6988-6991. https://doi.org/10.1039/C5CC01545F

[15] M. Juneau, M. Vonglis, J. Hartvigsen, L. Frost, D. Bayerl, M. Dixit, G. Mpourmpakis, J.R. Morse, J.W. Baldwin, H.D. Willauer, M.D. Porosoff, Assessing the viability of K-Mo_2C for reverse water-gas shift scale-up: molecular to laboratory to pilot scale, Energy Environ. Sci. 13 (2020) 2524-2539. https://doi.org/10.1039/D0EE01457E

[16] A. Pajares, X. Liu, J.R. Busacker, P. Ramírez de la Piscina, N. Homs, Supported nanostructured Mo_xC materials for the catalytic reduction of CO_2 through the reverse water gas shift reaction, Nanomaterials 12 (2022) 3165. https://doi.org/10.3390/nano12183165

[17] X. Liu, A. Pajares, D.D.C. Matienzo, P. Ramírez de la Piscina, N. Homs, Preparation and characterization of bulk Mo_xC catalysts and their use in the reverse water-gas shift reaction, Catal. Today, 356 (2020) 384-389. https://doi.org/10.1016/j.cattod.2019.11.011

[18] X. Liu, C. Kunkel, P. Ramírez de la Piscina, N. Homs, F. Viñes, F. Illas, Effective and highly selective CO generation from CO_2 using a polycrystalline α-Mo_2C catalyst, ACS Catal. 7 (2017) 4323-4335. https://doi.org/10.1021/acscatal.7b00735

[19] S. Posada-Pérez, P.J. Ramírez, J. Evans, F. Viñes, P. Liu, F. Illas, J.A. Rodriguez, Highly active Au/δ-MoC and Cu/δ-MoC catalysts for the conversion of CO_2: the metal/C ratio as a key factor defining activity, selectivity, and stability, J. Am. Chem. Soc. 138 (2016) 8269-8278. https://doi.org/10.1021/jacs.6b04529

[20] A. Pajares, H. Prats, A. Romero, F. Viñes, P. Ramírez de la Piscina, R. Sayós, N. Homs, F. Illas, Critical effect of carbon vacancies on the reverse water gas shift reaction over vanadium carbide catalysts, Appl. Catal. B-Environ. 267 (2020) 118719. https://doi.org/10.1016/j.apcatb.2020.118719

[21] Y. Ma, Z. Guo, Q. Jiang, K-H. Wu, H. Gong, Y. Liu, Molybdenum carbide clusters for thermal conversion of CO_2 to CO via reverse water-gas shift reaction, J. Energy Chem. 50 (2020) 37-43. https://doi.org/10.1016/j.jechem.2020.03.012

[22] J. Lefevere, S. Mullens, V. Meynen, The impact of formulation and 3D-printing on the catalytic properties of ZSM-5 zeolite, Chem. Eng. J. 349 (2018) 260-268. https://doi.org/10.1016/j.cej.2018.05.058

[23] S. Lawson, X. Li, H. Thakkar, A.A. Rownaghi, F. Rezaei, Recent advances in 3D printing of structured materials for adsorption and catalysis applications, Chem. Rev. 121 (2021) 6246-6291. https://doi.org/10.1021/acs.chemrev.1c00060

[24] C. Parra-Cabrera, C. Achille, S. Kuhn, R. Ameloot, 3D printing in chemical engineering and catalytic technology: structured catalysts, mixers and reactors, Chem. Soc. Rev. 47 (2018) 209-230. https://doi.org/10.1039/C7CS00631D

[25] L. Chatre, J. Socci, S.J. Adams, P. Denissenko, N. Cherkasov, Design of 3D-printed structures for improved mass transfer and pressure drop in packed-bed reactors, Chem. Eng. J. 420 (2021) 129762. https://doi.org/10.1016/j.cej.2021.129762

[26] V. Middelkoop, A. Vamvakeros, D. de Wit, S.D.M. Jacques, S. Danaci, C. Jacquot, Y. de Vos, D. Matras, S.W.T. Price, A.M. Beale, 3D printed Ni/Al_2O_3 based catalysts for CO_2 methanation – a comparative and operando XRD-CT study, J CO_2 util. 33 (2019) 478-487. https://doi.org/10.1016/j.jcou.2019.07.013

[27] C. Zang, L. McKeon, M.P. Kremer, S-H. Park, O. Ronan, A. Seral-Ascaso, S. Barwich, C.Ó. Coileáin, N. McEvoy, H.C. Nerl, B. Anasori, J.N. Coleman, Y. Gogotsi, V. Nicolosi, Additive-free MXene inks and direct printing of micro-supercapacitors, Nat. Commun. 10 (2019) 1795. https://doi.org/10.1038/s41467-019-09398-1

[28] W. Yang, J. Yang, J.J. Byun, F.P. Moissinac, J. Xu, S.J. Haigh, M. Domingos, M.A. Bissett, R.A.W. Dryfe, S. Barg, 3D printing of freestanding MXene architectures for current-collector-free supercapacitors, Adv. Mat. 31 (2019) 1902725. https://doi.org/10.1002/adma.201902725

[29] K. Li, J. Zhao, A. Zhussupbekova, C.E. Shuck, L. Hughes, Y. Dong, S. Barwich, S. Vaesen, I.V. Shvets, M. Möbius, W. Schmitt, Y. Gogotsi, V. Nicolosi, 4D printing of MXene hydrogels for high-efficiency pseudocapacitive energy storage, Nat. Commun. 13 (2022) 6884 https://doi.org/10.1038/s41467-022-34583-0

[30] K. Li, M. Liang, H. Wang, X. Wang, Y. Huang, J. Coelho, S. Pinilla, Y. Zhang, F. Qi, V. Nicolosi, Y. Xu, 3D MXene architectures for efficient energy storage and conversion, Adv. Funct. Mater. 30 (2020) 2000842. https://doi.org/10.1002/adfm.202000842

[31] M. Nagai, K. Oshikawa, T. Kurakami, T. Miyao, S. Omi, Surface properties of carbided molybdena-alumina and its activity for CO_2 hydrogenation, J. Catal. 180 (1998) 14-23. https://doi.org/10.1006/jcat.1998.2262

[32] A. M'Barki, L. Bocquet, A. Stevenson, Linking rheology and printability for dense and strong ceramics by direct ink writing, Sci. Rep. 7 (2017) 6017. https://doi.org/10.1038/s41598-017-06115-0

[33] L. del Mazo Barbara, M-P. Ginebra, Rheological characterisation of ceramic inks for 3D direct ink writing: A review, J. Eur. Ceram. Soc. 41 (2021) 18-33. https://doi.org/10.1016/j.jeurceramsoc.2021.08.031

[34] Y. Zheng, J. Song, X. Xu, M. He, Q. Wang, L. Yan, Peptization mechanism of boehmite and its effect on the preparation of a fluid catalytic cracking catalyst, Ind. Eng. Chem. Res. 53 (2014) 10029-10034. https://doi.org/10.1021/ie501060g

[35] K. Kennes, A. Kubarev, C. Demaret, L. Treps, O. Delpoux, M. Rivallan, E. Guillon, A. Méthivier, T. de Bruin, A. Gomez, B. Harbuzaru, M.B.J. Roeffaers, C. Chizallet, Multiscale visualization and quantification of the effect of binders on the acidity of shaped zeolites, ACS Catal. 12 (2022) 6794-6808. https://doi.org/10.1021/acscatal.2c02152

[36] C. Hutter, A. Zenklusen, S. Kuhn, Ph.R. Von Rohr, Large eddy simulation of flow through a streamwise-periodic structure, Chem. Eng. Sci. 66 (2011) 519-529. https://doi.org/10.1016/j.ces.2010.11.015

[37] C. Ferroni, M. Bracconi, M. Ambrosetti, M. Maestri, G. Groppi, E. Tronconi, A fundamental investigation of gas/solid heat and mass transfer in structured catalysts based on periodic open cellular structures (POCS), Ind. Eng. Chem. Res. 60 (2021) 10522-10538. https://doi.org/10.1021/acs.iecr.1c00215

[38] A. Shrestha, X. Gao, J.C. Hicks, C. Paolucci, Nanoparticle size effects on phase stability for molybdenum and tungsten carbides, Chem. Mater. 33 (2021) 4606-4620. https://doi.org/10.1021/acs.chemmater.1c01120

[39] P. Arnoldy, J.C.M. De Jonge, J.A. Moulijn, Temperature-programed reduction of molybdenum (VI) oxide and molybdenum (IV) oxide, J. Phys. Chem. 89 (1985) 4517-4526. https://doi.org/10.1021/j100267a021

[40] K. Oshikawa, M. Nagai, S. Omi, Characterization of molybdenum carbides for methane reforming by TPR, XRD, and XPS, J. Phys. Chem. B 105 (2001) 9124-9131. https://doi.org/10.1021/jp0111867

[41] G. Wang, J.A. Schaidle, M.B. Katz, Y. Li, X. Pan, L.T. Thompson, Alumina supported Pt-Mo_2C catalysts for the water-gas shift reaction, J. Catal. 304 (2013) 92-99. https://doi.org/10.1016/j.jcat.2013.04.007

[42] K. Murugappan, E.M. Anderson, D. Teschner, T.E. Jones, K. Skorupska, Y. Román-Leshkov, Operando NAP-XPS unveils differences in MoO_3 and Mo_2C during hydrodeoxygenation. Nat. Catal. 1 (2018) 960-967. https://doi.org/10.1038/s41929-018-0171-9

[43] L. Leclercq, A. Almazouari, M. Dufour, G. Leclercq, Carbide-oxide interactions in bulk and supported tungsten carbide catalysts for alcohol synthesis, in: S.T. Oyama (Ed.), The Chemistry of Transition Metal Carbides and Nitrides, Springer, Dordrecht, 1996, pp. 345-361. https://doi.org/10.1007/978-94-009-1565-7_18

[44] S. Posada-Pérez, F. Viñes, P.J. Ramírez, A.B. Vidal, J.A. Rodríguez, F. Illas, The bending machine: CO_2 activation and hydrogenation on δ-MoC(001) and β-Mo_2C(001) surfaces, Phys. Chem. Chem. Phys. 16 (2014) 14912. https://doi.org/10.1039/C4CP01943A

[45] Q. Bao, T. Bu, J. Yan, C. Zhang, C. Ning, Y. Zhang, M. Hao, W. Zhang, Z. Wang, Synthesis of methyl acrylate by aldol condensation of methyl acetate with formaldehyde over Al_2O_3-supported barium catalyst, Catal. Lett. 147 (2017) 1540-1550. https://doi.org/10.1007/s10562-017-2014-8

[46] W. Marquart, S. Raseale, M. Claeys, N. Fischer, Promoted Mo_xC_y-based catalysts for the CO_2 oxidative dehydrogenation of ethane, ChemCatChem 14 (2022) e202200267. https://doi.org/10.1002/cctc.202200267

[47] A. Davydov, The nature of oxide surface centers, in: A. Davydov (Ed.), Molecular Spectroscopy of Oxide Catalyst Surfaces, John Wiley & Sons, Hoboken, 2003, pp. 27-179. https://doi.org/10.1002/0470867981

[48] K. Zhao, L. Wang, M. Calizzi, E. Moioli, A. Züttel, In situ control of the adsorption species in CO_2 hydrogenation: Determination of intermediates and byproducts, J. Phys. Chem. C 122 (2018) 20888-20893. https://doi.org/10.1021/acs.jpcc.8b06508

[49] X. Wang, H. Shi, J. Hun-Kwak, J. Szanyi, Mechanism of CO_2 hydrogenation on Pd/Al_2O_3 catalysts: Kinetics and transient DRIFTS-MS studies, ACS Catal. 5 (2015) 6337-6349. https://doi.org/10.1021/acscatal.5b01464

[50] L.F. Bobadilla, J.L. Santos, S. Ivanova, J.A. Odriozola, A. Urakawa, Unravelling the role of oxygen vacancies in the mechanism of the reverse water-gas shift reaction by Operando DRIFTS and ultraviolet-visible spectroscopy, ACS Catal. 8 (2018) 7455-7467. https://doi.org/10.1021/acscatal.8b02121

[51] F.C. Meunier, D. Reid, A. Goguet, S. Shekhtman, C. Hardacre, R. Burch, W. Deng, M. Flytzani-Stephanopoulos, Quantitative analysis of the reactivity of formate species seen by DRIFTS over a $Au/Ce(La)O_2$ water-gas shift catalyst: First unambiguous evidence of the minority role of formates as reaction intermediates, J. Catal. 247 (2007) 277-287. https://doi.org/10.1016/j.jcat.2007.02.013

[52] W. Wu, Z. Wu, C. Liang, P. Ying, Z. Feng, C. Li, An IR study on the surface passivation of Mo_2C/Al_2O_3 catalyst with O_2, H_2O and CO_2, Phys. Chem. Chem. Phys. 6 (2004) 5603-5608. https://doi.org/10.1039/B411849A

[53] H. Tominaga, M. Nagai, Density functional study of carbon dioxide hydrogenation on molybdenum carbide and metal, Appl. Catal. A-Gen. 282 (2005) 5-13. https://doi.org/10.1016/j.apcata.2004.09.041

[54] M. Figueras, R.A. Gutiérrez, F. Viñes, P.J. Ramírez, J.A. Rodriguez, F. Illas, Supported molybdenum carbide nanoparticles as an excellent catalyst for CO_2 hydrogenation, ACS Catal. 11 (2021) 9679-9687. https://doi.org/10.1021/acscatal.1c01738

Appendix A. Supplementary material

The following supplementary information related to this article can be found in the online version at DOI

Supplementary Figures

Figure S1. 3D-printer used for the preparation of 3D structures.

Figure S2. 3D printing design of structures. (a) Top view. (b) Side view. (c) Perspective view.

Figure S3. XRD patterns of samples prepared from the thermal treatment of $(NH_4)Mo_7O_{24}$ and MoO_3 at different temperatures (973, 1073 and 1173 K) under a carburization atmosphere, $CH_4/H_2/He$=1/4/4, for 4 h (2.5 K min^{-1}) (a) XRD patterns of samples prepared using $(NH_4)Mo_7O_{24}$. (b) XRD patterns of samples prepared using MoO_3. (c) XRD reference patterns of hexagonal β-Mo_2C and orthorhombic α-Mo_2C (Intensity multiplied by 100).

Figure S4. Rheological behavior of the pastes. (a) Viscosity of the different inks determined from rotational measurement between 0.01 and 100 s^{-1}. (b) Rheological behavior of the different pastes determined using an amplitude sweep at 1 Hz, storage modulus (G') and loss modulus (G''). Only rheology tests of Al_2O_3, 1MoAl, 10MoAl and 30MoAl pastes were plotted for a better visualization.

Figure S5. General scheme of the preparation of 3D-Mo_xC/Al_2O_3 monoliths.

Figure S6. Microscopy and EDX analysis of 1MoAl. (a) OM images and fiber measurement. (b) SEM images. (c) TEM and HRTEM images, and particle size distribution (inset). (d) STEM image, EDX spectrum and mapping analysis. Cu EDX peaks correspond to the TEM grid.

Figure S7. Microscopy and EDX analysis of 5MoAl. (a) OM images and fiber measurement. (b) SEM images. (c) TEM and HRTEM images, and particle size distribution (inset). (d) STEM image, EDX spectrum and mapping analysis. Cu EDX peaks correspond to the TEM grid.

Figure S8. Microscopy and EDX analysis of 20MoAl. (a) OM images and fiber measurement. (b) SEM images. (c) TEM and HRTEM images, and particle size distribution (inset). (d) STEM image, EDX spectrum and mapping analysis. Cu EDX peaks corresponds to the TEM grid.

Figure S9. Microscopy and EDX analysis of 30MoAl. (a) OM images and fiber measurement. (b) SEM images. (c) TEM and HRTEM images, and particle size distribution (inset). (d) STEM image, EDX spectrum and mapping analysis. Cu EDX peaks corresponds to the TEM grid.

Figure S10. Microscopy and EDX analysis of Al_2O_3 monolith. (a) OM images and fiber measurement. (b) SEM images. (c) SEM cross-section image. (d) Representative EDX spectrum.

Figure S11. Stress-strain characterization of Mo_xC/Al_2O_3 monoliths. (a) Stress-strain curves. (b) Setup used for the stress tests.

Figure S12. N_2 adsorption-desorption isotherms and porous size distribution (inset) of Mo_xC/Al_2O_3 monoliths and Mo_2C.

Figure S13. Characterization of Mo_xC/Al_2O_3 monoliths by Hg porosimetry.

Figure S14. XPS analysis of Mo_xC/Al_2O_3 monoliths. (a) C 1s XPS level. (b) O 1s XPS level. (c) Al 2p XPS level.

Figure S15. Raman spectra of Mo_xC/Al_2O_3 monoliths.

Figure S16. CO_2-TPD of Mo_xC/Al_2O_3 monoliths and Mo_2C sample. The intensities were normalized by the catalyst mass.

Figure S17. Catalytic results in the RWGS reaction over 10MoAl and 30MoAl. (a) CO_2 conversion (b) Arrhenius plot in the 673-823 K range. Reaction conditions: m_{cat}=0.75 g, $CO_2/H_2/N_2$=1/3/3, GHSV=12000 h^{-1} and P=0.1 MPa.

Figure S18. Catalytic behavior of 10MoAl in the RWGS reaction using a $CO_2/H_2/N_2$=1/3/3 and 1/1/3 molar ratio. (a) CO_2 conversion. (b) CO selectivity. Reaction conditions: P=0.1 MPa, m_{cat}=0.75 g, GHSV=4000 h^{-1} and T=523-873 K.

Figure S19. XRD patterns of spent Mo_xC/Al_2O_3 monoliths after RWGS reaction ($CO_2/H_2/N_2$=1/3/3, P=0.1 MPa, T=523-873 K and GHSV=4000 h^{-1}).

Figure S20. XRD pattern of spent 10MoAl sample after RWGS reaction ($CO_2/H_2/N_2$=1/1/3, P=0.1 MPa, T=523-873 K and GHSV=4000 h^{-1}).

Figure S21. N_2 adsorption-desorption isotherms and porous size distribution (inset) of spent Mo_xC/Al_2O_3 monoliths ($CO_2/H_2/N_2$=1/3/3, T=523-873 K, P=0.1 MPa and GHSV=4000 h^{-1}). 10MoAl_5days: 10MoAl after 5 days at 873 K under RWGS reaction ($CO_2/H_2/N_2$=1/3/3, P=0.1 MPa and GHSV=4000 h^{-1}). 10MoAl_1/1: 10MoAl after RWGS reaction ($CO_2/H_2/N_2$=1/1/3, T=523-873 K, P=0.1 MPa and GHSV=4000 h^{-1}).

Figure S22. Characterization of 10MoAl after 5 days at 873 K under RWGS reaction ($CO_2/H_2/N_2$=1/3/3, P=0.1 MPa and GHSV=4000 h^{-1}). (a) XRD pattern. (b) OM image. (c) and (d) SEM images. (e) Representative EDX spectrum.

Figure S23. DRIFT spectra of samples recorded under RWGS conditions after a H_2 pretreatment at 723 K: (a) Al_2O_3, (b) 5MoAl, (c) 10MoAl, (d) 30MoAl, (e) δ-MoC and (f) α/β-Mo_2C. Conditions: 70 mL min^{-1}, CO_2/H_2/He=1/3/3, 523–673 K.

Figure S24. DRIFT spectra of 5MoAl under CO_2 and CO flow at (a) 308 K and (b) 523 K. Conditions: 70 mL min^{-1}, CO_2/He=1/4 or CO/He=1/4, 523–673 K.

Figure S25. Comparison of DRIFT spectra of 5MoAl (solid line) and Al_2O_3 (dotted line) under (a) CO_2 + H_2 and (b) followed by H_2 flow at different temperatures. The shaded areas correspond to the main types of intermediates observed: bicarbonates

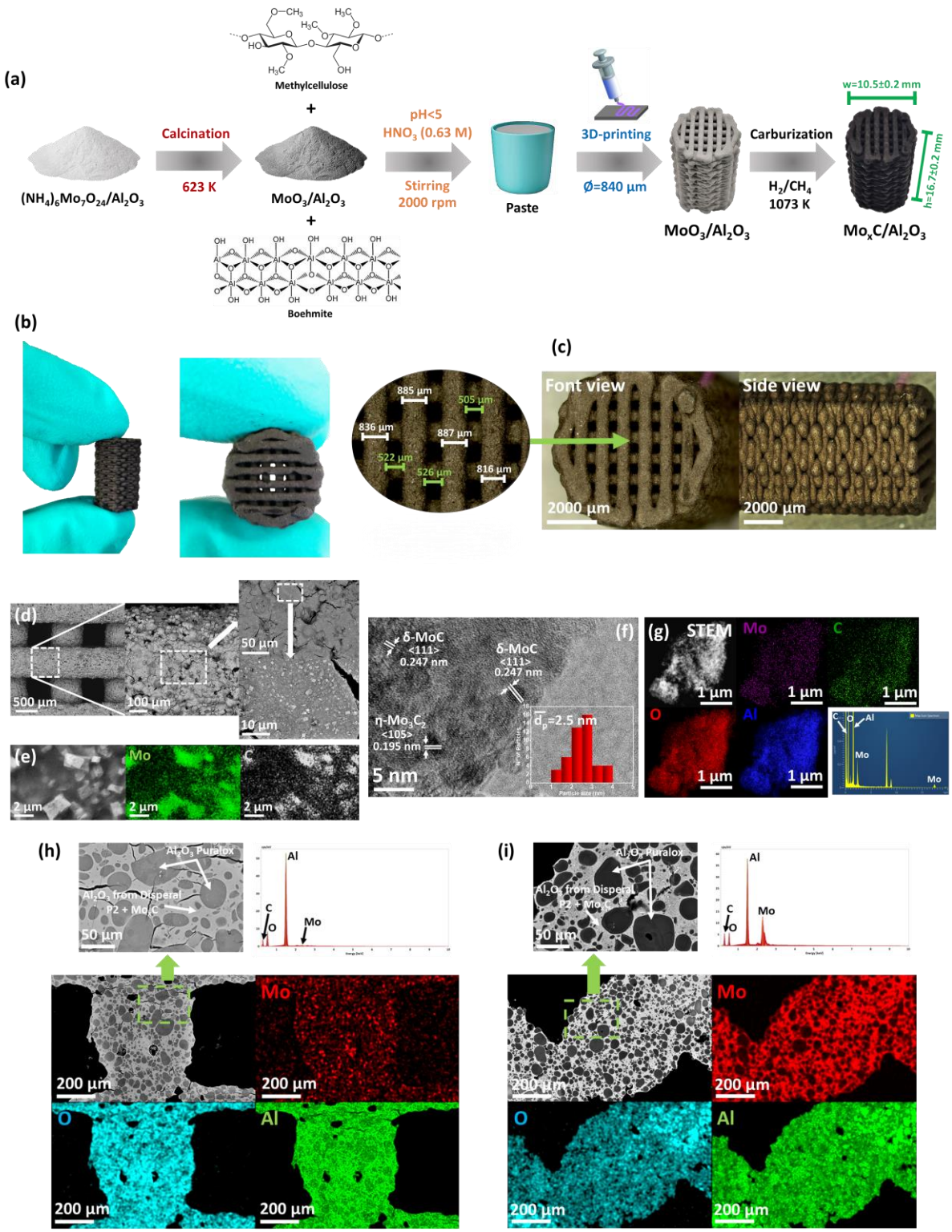

Figure 1. Preparation and microscopy characterization of 3D-printing Mo_xC/Al_2O_3 monoliths. (a) Preparation. (b-g) Microscopy characterization of 10MoAl: (b) Images; (c) OM images; (d) SEM images; (e) SEM-EDX mapping; (f) HRTEM image and particle size distribution (inset); (g) STEM image, EDX mapping and spectrum. (h) and (i) SEM cross-section images, EDX mapping and spectrum of 1MoAl and 30MoAl, respectively.

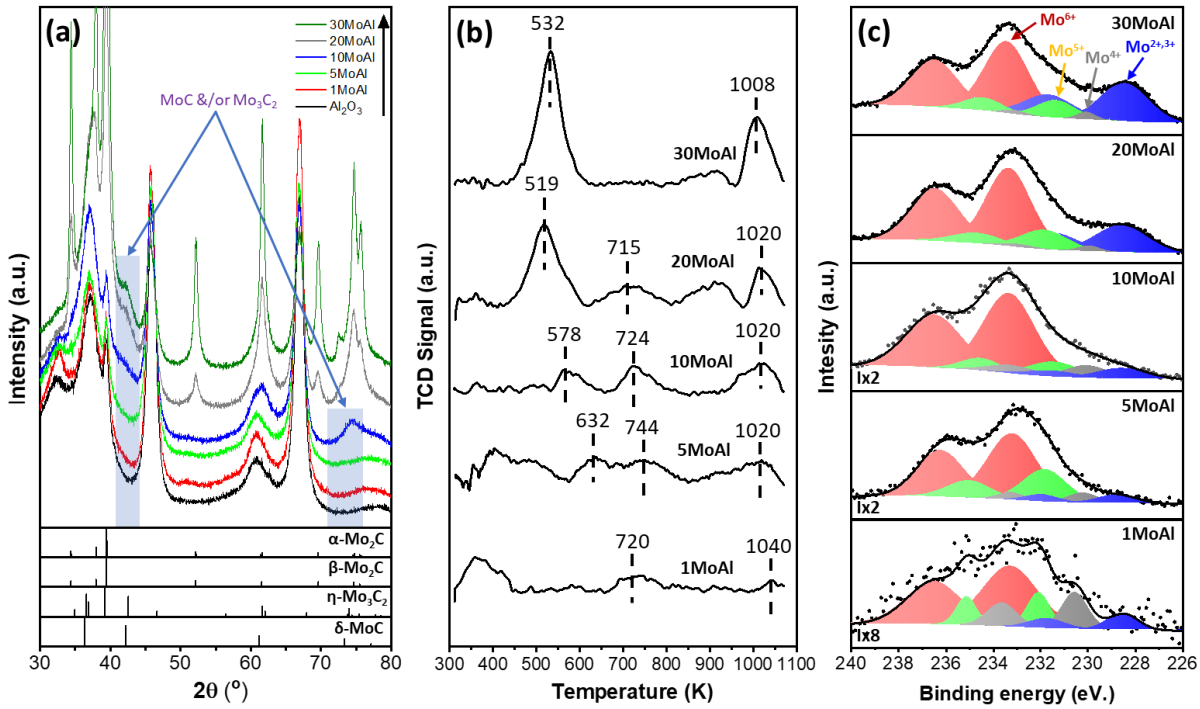

Figure 2. Characterization of Mo_xC/Al_2O_3 monoliths. (a) XRD patterns. (b) H_2-TPR profiles. (c) Mo 3d XP level spectra.

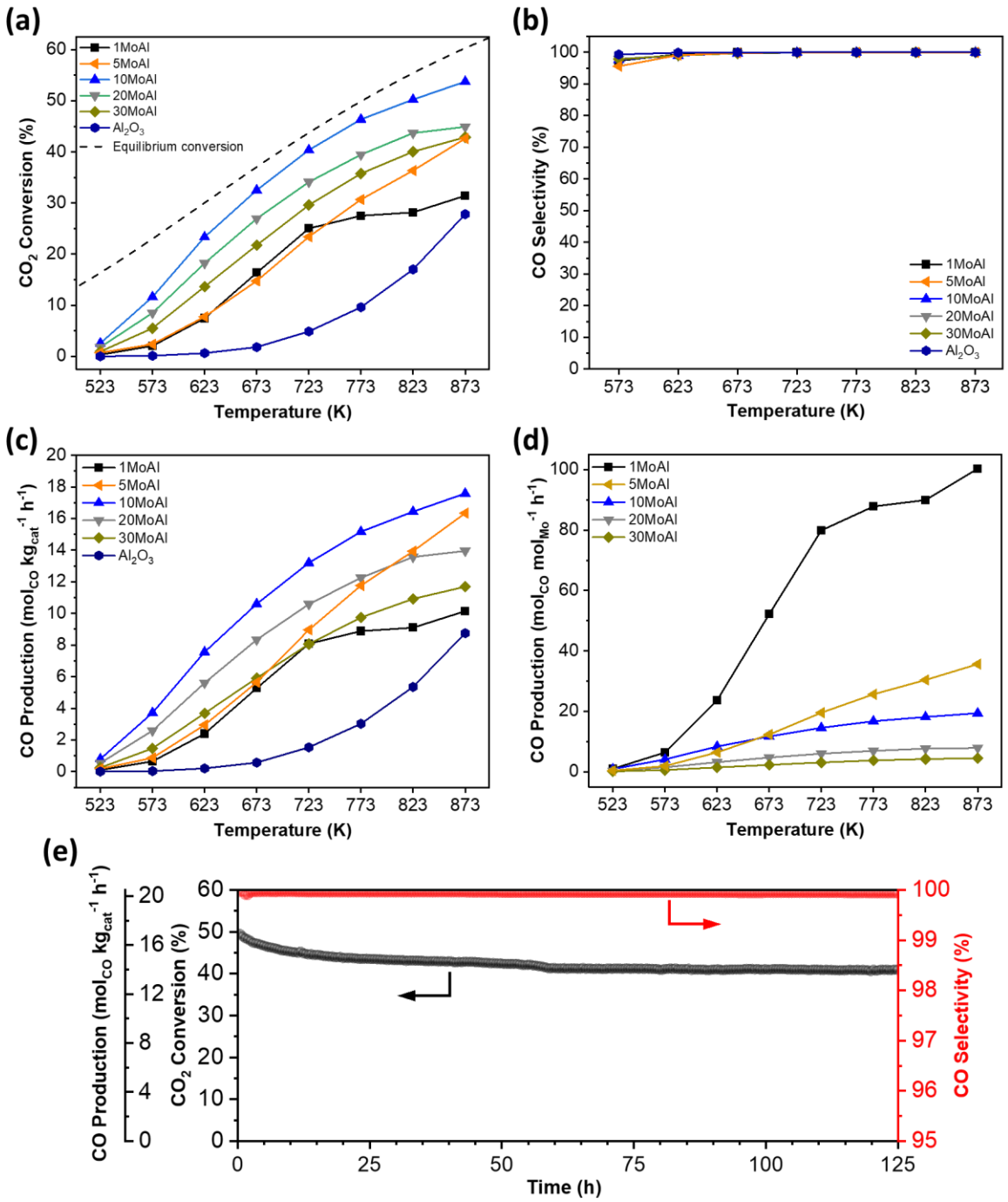

Figure 3. Catalytic behavior of Mo_xC/Al_2O_3 monoliths in the RWGS reaction. (a) CO_2 conversion. (b) CO selectivity. (c) and (d) CO production. (e) Long-term catalytic test of 10MoAl in the RWGS reaction at 873 K for 5 days. Reaction conditions: P=0.1 MPa, m_{cat}=0.7-0.9 g, $CO_2/H_2/N_2$=1/3/3 and GHSV=4000 h^{-1}.

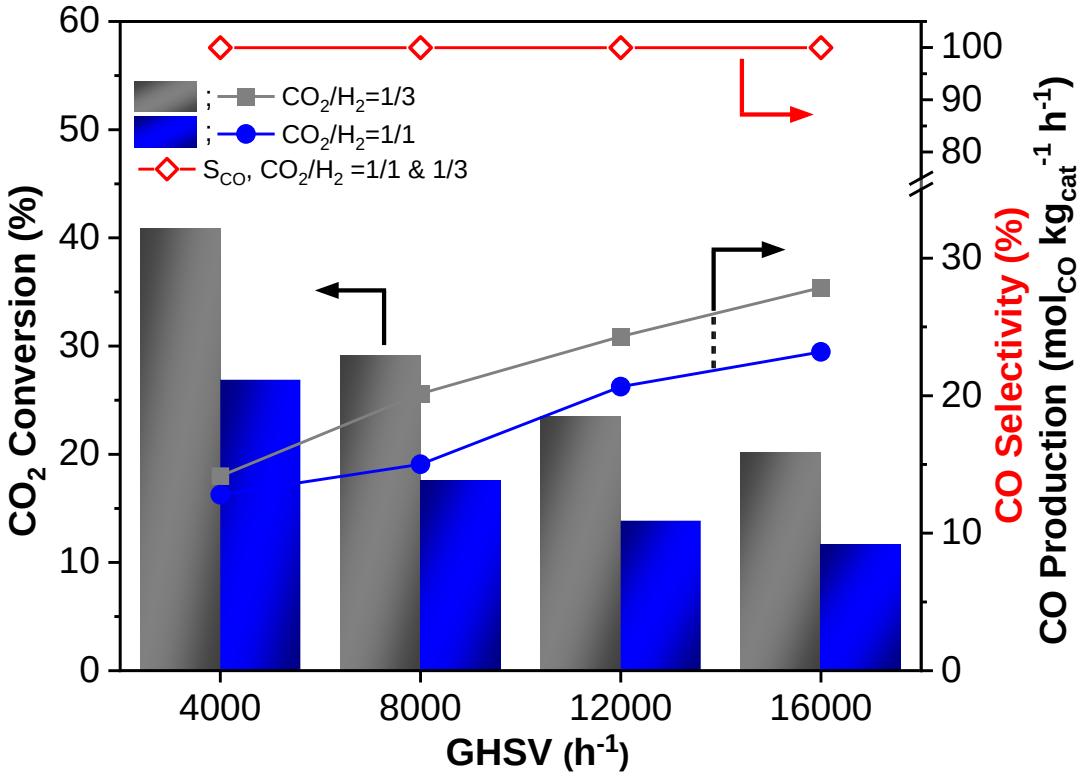

Figure 4. Catalytic behavior of 10MoAl under RWGS reaction at 873 K and different GHSV using a $CO_2/H_2/N_2$=1/3/3 & 1/1/3 molar ratio. The catalyst was first under reaction at 4000 h^{-1} during five days. Reaction conditions: P=0.1 MPa and m_{cat}=0.75 g. Gray and blue bars correspond to the CO_2 conversion using a CO_2/H_2=1/3 & 1/1, respectively. Gray and blue lines correspond to CO production using a CO_2/H_2=1/3 & 1/1, respectively. Red Line corresponds to CO selectivity for both CO_2/H_2=1/3 & 1/1.

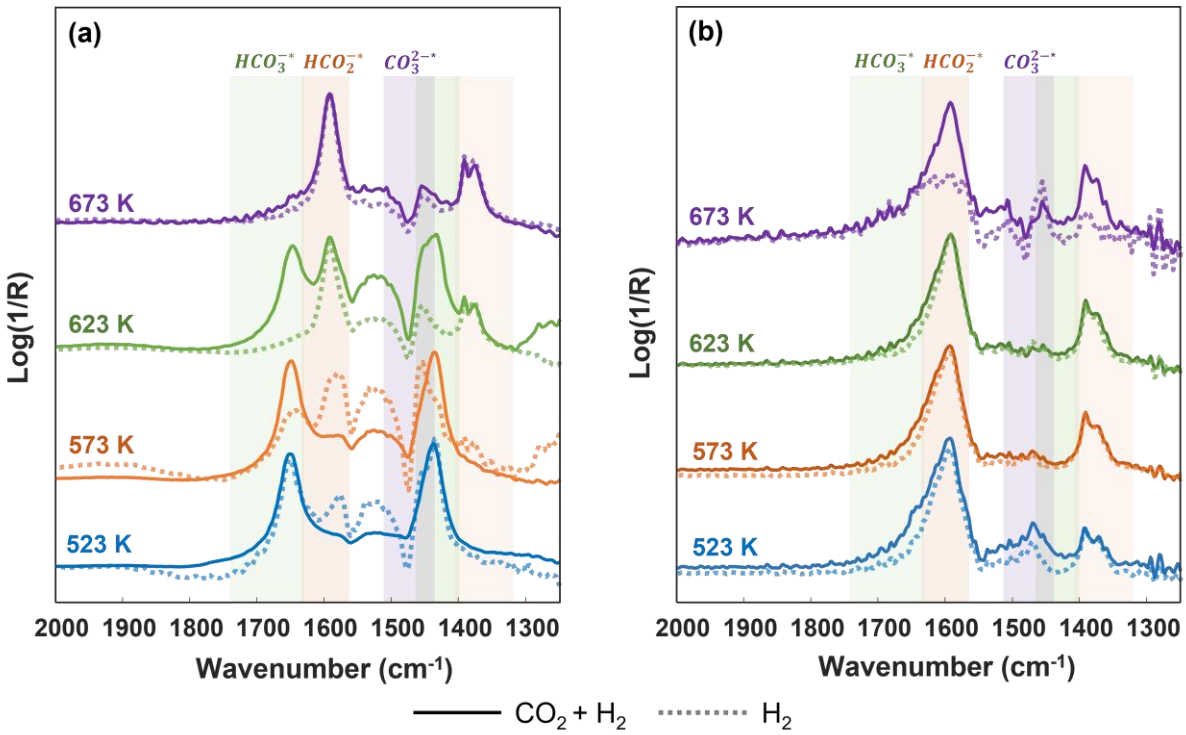

Figure 5. Operando DRIFT spectra of (a) Al_2O_3 and (b) 5MoAl, under CO_2 + H_2 flow (solid line) followed by H_2 flow (dotted line). Conditions: 70 mL min^{-1}, $CO_2/H_2/He$=1/3/3, or H_2/He=3/4, 523–673 K.

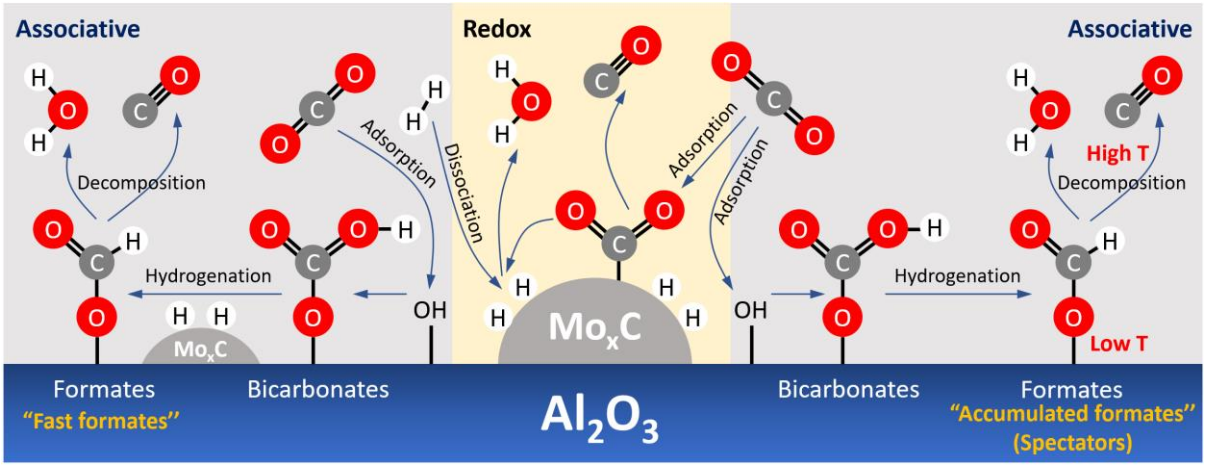

Figure 6. Proposed mechanism of RWGS reaction for Mo_xC/Al_2O_3 systems.

Table 1. Different characteristics of Mo_xC/Al_2O_3 monoliths.

Catalyst	Crystallite size of Mo_2C (XRD) (nm)	Particle size of Mo_xC (TEM) (nm)	S_{BET} ($m^2\ g^{-1}$)	Pore Volume ($cm^3\ g^{-1}$)		Main Pore size - BJH (nm)	Density ($g\ cm^{-3}$)	Stress (MPa)
				N_2 sorption	Hg intrusion			
1MoAl	-	<1	131	0.60	0.58	6.2	3.24	3.68
5MoAl	-	1.8	153	0.70	0.81	6.2	3.27	0.74
10MoAl	-	2.5	147	0.68	0.78	5.2	3.37	1.00
20MoAl	12.7	4.6[1] and 11.9[2]	116	0.63	0.53	5.1	3.60	2.10
30MoAl	19.0	6.4[1] and 18.5[2]	102	0.58	0.47	5.0	3.85	3.60
Al_2O_3	-	-	160	0.58	0.42	5.0	3.13	2.60
Mo_2C	40.0	-	3	0.01	-	18.1	-	-

[1]Mean particle size in 1st mode.[2]Mean particle size in 2nd mode.

Table 2. Chemical analysis (ICP) and surface characterization (XPS) of Mo_xC/Al_2O_3 monoliths.

Catalyst	Mo Content (wt.%)$_{ICP}$	$(Mo/Al)_{ICP}$	$(Mo/Al)_{XPS}$	Dispersion factor	$(Mo^{2+,3+}/Mo^{n+}_{total})_{XPS}$
1MoAl	1.0	0.006	0.009	1.6	0.09
5MoAl	4.4	0.028	0.069	2.5	0.06
10MoAl	8.7	0.061	0.065	1.1	0.08
20MoAl	17	0.133	0.074	0.6	0.23
30MoAl	25	0.227	0.096	0.4	0.30